ISDU-QSMNet: Iteration Specific Denoising with Unshared Weights for Improved QSM Reconstruction

Vaddadi Venkatesh, Raji Susan Mathew, and Phaneendra K. Yalavarthy

---

1 Dataset Details

A total of 60 scans acquired at 3 T (nine datasets using Tim Trio, and three datasets using MAGNETOM Skyra, Siemens Healthineers, Forchheim, Germany) from 12 healthy volunteers at five different head orientations were utilized in this work [1]. The acquisition parameters for the SNU dataset included a field of view (FOV) of 224 × 224 × 176 mm^3 for healthy volunteers scanned on a Skyra 3T scanner, a voxel size of 1 × 1 × 1 mm^3, a repetition time (TR) of 33 ms, an echo time (TE) of 25 ms, and a total acquisition time of 5 min 46 s (5 min 18 s for patients). Dataset-II was acquired at 7 T (Philips Achieva) with four head orientations each from eight healthy subjects, with a total of 32 volumes [2]. Three slightly different 3D GRE sequences were used to acquire the dataset with voxel size $= 1 \times 1 \times 1\ mm^3$. The other acquisition parameters are as follows: $TR = 28\ ms$, $TE1/\delta TE = 5/5\ ms$, 5 echoes, $FOV = 224 \times 224 \times 126\ mm^3$ for the first four subjects, $TR = 45\ ms$, $TE1/\delta TE = 2/2\ ms$, 9 echoes, $FOV = 224 \times 224 \times 110\ mm^3$ for next three subjects and $TR = 45\ ms$, $TE1/\delta TE = 2/2\ ms$, 16 echoes, $FOV = 224 \times 224 \times 110\ mm^3$ for the last subject [2]. Among the total 32 volumes, sixteen volumes were of matrix sizes 224 × 224 × 126, and the remaining sixteen volumes were of matrix size 224 × 224 × 110. Brain masks were generated from the magnitude images using the Brain Extraction Tool (BET) [3]. Laplacian phase unwrapping [4] was performed within the brain mask to extract the unwrapped phase. Subsequently, the background field was removed using Variable-kernel Sophisticated Harmonic Artifact Reduction for Phase data (V-SHARP) [5, 6] to generate the local field map. The rotated local field maps were registered with the local field map of the unrotated head orientation using rotation matrices (FLIRT [7, 8]). These rotation matrices were obtained by aligning the rotated magnitude images with the magnitude images of the unrotated head orientation. Finally, the COSMOS algorithm [9] was applied to the registered local fields to generate high-quality susceptibility maps, which served as the ground truth. The dataset-I and II were pre-processed and shared by Ref. [1] and Ref. [2], respectively.

2 Training Details for Reproducibility

The training configurations and hyperparameters used in this study are essential for reproducibility and can guide future development efforts. In this study, all comparison models were trained from scratch, and their training parameters were individually optimized to ensure a fair comparison across models.

All deep learning models were developed using Python and implemented in the PyTorch framework. The training was performed with a batch size of 8, a learning rate of 1×10^{-4}, and for a total of 25 epochs. The Adam optimizer was used for parameter updates. To evaluate performance, we experimented with two loss functions: the Mean Squared Error (MSE) loss and a combined loss, which integrates the L_1 norm of voxel-wise differences, L_1 norm of edge differences, and model loss (the L_1 norm of the difference between the input local field and the local field formed from the output QSM). Among the deep learning models, QSMNet achieved its best performance using the combined loss, while DeepQSM and xQSM performed best with the MSE loss. SpiNet-QSM and

LP-CNN are model-based deep learning frameworks used for QSM reconstruction. Both models were trained with a learning rate of 1×10^{-4}, a batch size of 2, and a combined loss function. SpiNet-QSM was trained for 45 epochs, while LP-CNN was trained for 80 epochs. Due to their model-based architecture involving iterative unrolling, both frameworks require significant training time, with each epoch taking approximately 120 minutes even for $K = 4$ iterations, highlighting the computational demands of such approaches.

The limited data and full data training experiments were conducted independently, with no knowledge transfer between them. For both scenarios, the models were trained from scratch using their respective datasets. Specifically, the weights obtained from the limited data experiments were not used to initialize the models in the full data experiments, and vice versa.

3 ROI Analysis using Limited data training models

To evaluate the regional accuracy and robustness of QSM reconstruction methods under limited training data conditions, we conducted a comprehensive region-of-interest (ROI) analysis across six distinct brain regions: Caudate (CAU), Putamen (PUT), Globus Pallidus (GP), Left and Right White Matter (LWM/RWM), and Left and Right Gray Matter (LGM/RGM). This evaluation was performed on six test subjects from the SNU dataset, with all models trained using only a reduced subset of the available training data. The analysis provides insights into how well each method preserves susceptibility values and structural integrity in clinically relevant regions, even in data-constrained training scenarios.

Table 1 reports, for each ROI and subject, both the mean susceptibility value (in ppm) and the corresponding Pearson correlation coefficient with COSMOS, which serves as the reference standard. Together, these metrics offer a comprehensive assessment of the reconstructed susceptibility maps in terms of absolute quantitative accuracy and structural consistency.

To highlight the best-performing models, the table uses bold formatting to indicate the susceptibility values with the smallest absolute deviation from the COSMOS ground truth, as well as the highest Pearson correlation coefficients within each subject's ROI. This combined evaluation effectively distinguishes methods that not only achieve anatomically accurate susceptibility estimates but also exhibit strong alignment with the COSMOS reference across various brain regions and subjects.

4 QSM Reconstruction on RC-1 and RC-2 Datasets

To assess the generalization of models trained on the SNU dataset, we evaluated QSM reconstructions on two external datasets: RC-1 and RC-2. Figure 1 and Figure 2 show representative susceptibility maps reconstructed from RC-1 and RC-2 data, respectively. The results demonstrate that the models maintain high reconstruction quality and consistency, emphasizing their robustness across different acquisition conditions.

5 QSM Reconstructions on SNU Test Subjects

Figures 3, 4, and 5 present QSM reconstructions for Subjects 7, 8, and 9 from the SNU test set, using models trained on the full SNU dataset. Each figure shows sagittal, coronal, and axial views of the COSMOS reference (top row), followed by reconstructions from various methods: SpiNet-QSM, LPCNN, QSMNet, DeepQSM, xQSM, ISDU-QSMNet-USW, and ISDU-QSMNet-USW-RS. Quantitative metrics—SSIM, PSNR, and HFEN—are included for each method, enabling both visual and numerical comparison of reconstruction performance across subjects.

Table 1: Comparison of susceptibility values (in ppm) and their correlations with COSMOS across eight ROIs: Caudate (CAU), Putamen (PUT), Globus Pallidus (GP), left/right White Matter (WM), and left/right Gray Matter (GM), derived from reconstructed susceptibility maps for six test subjects from the SNU dataset. All models were trained on limited training data from SNU dataset. For each subject's ROI, the best-performing method (i.e., susceptibility value with the smallest deviation from COSMOS and highest correlation coefficient) is highlighted in bold.

	Susceptibility values						Correlation with COSMOS					
METHOD	**sub-1**	**sub-2**	**sub-3**	**sub-4**	**sub-5**	**sub-6**	**sub-1**	**sub-2**	**sub-3**	**sub-4**	**sub-5**	**sub-6**
ROI: CAUDATE												
COSMOS	0.041 ± 0.027	0.036 ± 0.034	0.036 ± 0.023	0.038 ± 0.025	0.052 ± 0.033	0.044 ± 0.023	1.000	1.000	1.000	1.000	1.000	1.000
SpiNet-QSM	0.056 ± 0.029	0.049 ± 0.033	0.040 ± 0.027	0.042 ± 0.027	0.065 ± 0.035	0.061 ± 0.024	0.926	0.897	**0.863**	**0.891**	0.925	**0.933**
LPCNN	0.046 ± 0.028	0.043 ± 0.027	0.043 ± 0.025	0.041 ± 0.025	0.066 ± 0.032	0.058 ± 0.023	0.888	0.846	0.822	0.860	0.900	0.891
QSMnet	0.028 ± 0.023	0.027 ± 0.027	0.031 ± 0.024	0.028 ± 0.025	0.046 ± 0.033	0.038 ± 0.025	0.891	0.865	0.817	0.832	0.865	0.879
DeepQSM	0.029 ± 0.022	0.032 ± 0.024	0.029 ± 0.023	0.029 ± 0.024	0.048 ± 0.031	0.039 ± 0.024	0.885	0.793	0.777	0.809	0.844	0.853
STAR-QSM	0.049 ± 0.030	0.033 ± 0.040	**0.039 ± 0.028**	0.033 ± 0.026	**0.050 ± 0.038**	0.047 ± 0.025	0.864	0.850	0.816	0.864	0.851	0.859
NDI	0.034 ± 0.022	0.025 ± 0.028	0.029 ± 0.022	0.026 ± 0.020	0.037 ± 0.025	**0.041 ± 0.021**	0.881	0.846	0.812	0.837	0.834	0.848
ISDU-QSMNet-USW	**0.045 ± 0.027**	0.041 ± 0.029	**0.039 ± 0.026**	**0.039 ± 0.025**	0.055 ± 0.032	0.049 ± 0.026	**0.931**	**0.905**	0.833	0.882	**0.934**	0.917
ROI: PUTAMEN												
COSMOS	0.033 ± 0.027	0.047 ± 0.036	0.040 ± 0.028	0.051 ± 0.030	0.071 ± 0.037	0.043 ± 0.026	1.000	1.000	1.000	1.000	1.000	1.000
SpiNet-QSM	0.046 ± 0.032	0.060 ± 0.038	0.057 ± 0.032	0.066 ± 0.032	0.084 ± 0.040	0.063 ± 0.027	0.928	0.901	0.904	0.892	0.919	0.924
LPCNN	0.041 ± 0.030	0.058 ± 0.032	0.052 ± 0.028	0.058 ± 0.028	0.075 ± 0.032	0.058 ± 0.025	0.892	0.882	0.886	0.883	0.887	0.887
QSMnet	**0.032 ± 0.030**	**0.046 ± 0.035**	**0.042 ± 0.030**	0.047 ± 0.029	0.056 ± 0.036	**0.048 ± 0.029**	0.888	0.862	0.877	0.896	0.899	0.896
DeepQSM	0.036 ± 0.030	0.055 ± 0.037	0.046 ± 0.031	**0.051 ± 0.031**	0.066 ± 0.037	0.050 ± 0.029	0.867	0.857	0.871	0.886	0.895	0.881
STAR-QSM	0.023 ± 0.028	0.031 ± 0.034	0.035 ± 0.029	0.040 ± 0.029	0.051 ± 0.036	0.035 ± 0.025	0.892	0.842	0.850	0.879	0.855	0.868
NDI	0.023 ± 0.024	0.037 ± 0.030	0.032 ± 0.027	0.035 ± 0.026	0.047 ± 0.029	0.037 ± 0.025	0.865	0.874	0.864	0.877	0.866	0.881
ISDU-QSMNet-USW	0.039 ± 0.030	0.051 ± 0.034	0.046 ± 0.029	0.052 ± 0.029	**0.068 ± 0.035**	0.050 ± 0.027	**0.934**	**0.919**	**0.912**	**0.903**	**0.926**	**0.926**
ROI: GLOBUS PALLIDUS												
COSMOS	0.128 ± 0.040	0.153 ± 0.062	0.129 ± 0.046	0.128 ± 0.044	0.167 ± 0.056	0.125 ± 0.038	1.000	1.000	1.000	1.000	1.000	1.000
SpiNet-QSM	0.147 ± 0.043	0.170 ± 0.058	0.151 ± 0.049	0.152 ± 0.047	**0.174 ± 0.055**	0.150 ± 0.041	0.918	0.919	0.932	0.920	0.925	0.930
LPCNN	0.126 ± 0.037	0.140 ± 0.048	0.128 ± 0.044	0.127 ± 0.041	0.142 ± 0.048	**0.124 ± 0.037**	0.918	0.876	0.924	0.931	0.884	0.921
QSMnet	0.126 ± 0.036	0.135 ± 0.050	**0.129 ± 0.041**	**0.129 ± 0.041**	0.143 ± 0.048	0.135 ± 0.038	0.836	0.856	0.910	0.893	0.882	0.890
DeepQSM	**0.128 ± 0.038**	0.138 ± 0.052	0.131 ± 0.042	0.129 ± 0.042	0.144 ± 0.050	0.120 ± 0.038	0.828	0.879	0.890	0.884	0.849	0.841
STAR-QSM	0.096 ± 0.037	0.112 ± 0.054	0.106 ± 0.043	0.102 ± 0.040	0.122 ± 0.052	0.102 ± 0.035	0.867	0.868	0.865	0.891	0.823	0.891
NDI	0.086 ± 0.029	0.105 ± 0.042	0.093 ± 0.036	0.090 ± 0.034	0.101 ± 0.038	0.102 ± 0.032	0.860	0.871	0.871	0.860	0.808	0.897
ISDU-QSMNet-USW	0.138 ± 0.040	**0.156 ± 0.052**	0.140 ± 0.047	0.140 ± 0.045	0.156 ± 0.052	0.140 ± 0.041	**0.942**	**0.919**	**0.949**	**0.947**	**0.928**	**0.943**
ROI: LEFT WHITE MATTER												
COSMOS	−0.010 ± 0.023	−0.007 ± 0.023	−0.005 ± 0.025	−0.008 ± 0.021	−0.009 ± 0.026	−0.007 ± 0.021	1.000	1.000	1.000	1.000	1.000	1.000
SpiNet	**-0.010 ± 0.023**	**-0.006 ± 0.022**	**-0.006 ± 0.025**	**-0.009 ± 0.020**	**-0.009 ± 0.023**	−0.004 ± 0.020	0.908	**0.871**	0.903	0.867	0.884	**0.891**
LPCNN	−0.013 ± 0.022	−0.008 ± 0.021	−0.007 ± 0.024	−0.012 ± 0.019	−0.011 ± 0.023	−0.006 ± 0.020	0.887	0.863	0.896	0.859	0.870	0.877
QSMNet	−0.009 ± 0.021	−0.006 ± 0.020	−0.004 ± 0.023	−0.007 ± 0.020	−0.005 ± 0.022	−0.008 ± 0.020	0.870	0.841	0.891	0.844	0.863	0.835
DeepQSM	−0.009 ± 0.020	−0.006 ± 0.019	−0.004 ± 0.022	−0.006 ± 0.019	−0.005 ± 0.021	−0.007 ± 0.019	0.859	0.836	0.873	0.834	0.847	0.857
starQSM	−0.007 ± 0.025	−0.003 ± 0.026	−0.002 ± 0.027	−0.005 ± 0.023	−0.006 ± 0.028	−0.004 ± 0.024	0.834	0.814	0.821	0.841	0.821	0.830
NDI	−0.008 ± 0.021	−0.004 ± 0.022	−0.003 ± 0.022	−0.006 ± 0.019	−0.006 ± 0.021	−0.005 ± 0.021	0.860	0.822	0.837	0.830	0.818	0.849
ISDU-QSMNet-USW	-0.011 ± 0.021	**-0.006 ± 0.020**	**-0.006 ± 0.024**	**-0.008 ± 0.019**	**-0.009 ± 0.022**	**-0.006 ± 0.019**	**0.914**	0.870	**0.914**	**0.879**	**0.898**	0.887
ROI: RIGHT WHITE MATTER												
COSMOS	−0.006 ± 0.032	−0.003 ± 0.026	−0.004 ± 0.028	−0.005 ± 0.030	−0.007 ± 0.034	−0.004 ± 0.028	1.000	1.000	1.000	1.000	1.000	1.000
SpiNet	−0.005 ± 0.032	−0.004 ± 0.025	−0.004 ± 0.029	−0.005 ± 0.028	−0.006 ± 0.031	−0.002 ± 0.029	0.929	0.884	0.909	0.916	0.917	**0.920**
LPCNN	−0.009 ± 0.030	−0.006 ± 0.024	−0.006 ± 0.028	−0.008 ± 0.027	−0.009 ± 0.030	−0.004 ± 0.027	0.913	0.867	0.911	0.903	0.906	0.906
QSMNet	−0.004 ± 0.027	−0.004 ± 0.022	−0.003 ± 0.026	−0.004 ± 0.025	−0.004 ± 0.027	−0.004 ± 0.026	0.901	0.846	0.894	0.897	0.885	0.889
DeepQSM	−0.005 ± 0.028	−0.004 ± 0.022	−0.003 ± 0.026	−0.004 ± 0.024	−0.004 ± 0.027	−0.004 ± 0.025	0.901	0.845	0.886	0.893	0.880	0.888
starQSM	−0.003 ± 0.032	−0.002 ± 0.028	−0.001 ± 0.030	−0.002 ± 0.029	−0.005 ± 0.033	−0.002 ± 0.030	0.871	0.823	0.840	0.884	0.841	0.868
NDI	−0.004 ± 0.026	−0.003 ± 0.023	−0.003 ± 0.025	−0.003 ± 0.024	−0.005 ± 0.025	−0.003 ± 0.027	0.876	0.821	0.852	0.869	0.835	0.889
ISDU-QSMNet-USW	**-0.007 ± 0.029**	-0.004 ± 0.023	**-0.004 ± 0.027**	-0.006 ± 0.026	**-0.007 ± 0.029**	**-0.004 ± 0.027**	**0.935**	**0.888**	**0.924**	**0.922**	**0.923**	0.919
ROI: LEFT GRAY MATTER												
COSMOS	0.002 ± 0.022	−0.001 ± 0.024	−0.001 ± 0.020	0.000 ± 0.019	0.002 ± 0.025	−0.001 ± 0.020	1.000	1.000	1.000	1.000	1.000	1.000
SpiNet	0.003 ± 0.018	0.001 ± 0.019	0.001 ± 0.016	0.000 ± 0.015	0.002 ± 0.019	0.002 ± 0.016	0.848	0.837	0.822	**0.824**	0.842	**0.846**
LPCNN	0.001 ± 0.018	0.000 ± 0.019	−0.001 ± 0.016	−0.002 ± 0.015	0.000 ± 0.019	0.001 ± 0.016	0.814	0.812	0.799	0.785	0.818	0.825
QSMNet	0.002 ± 0.017	0.002 ± 0.018	0.002 ± 0.015	0.002 ± 0.015	0.004 ± 0.018	0.000 ± 0.016	0.792	0.805	0.786	0.773	0.807	0.803
DeepQSM	0.001 ± 0.016	0.001 ± 0.017	0.001 ± 0.015	0.001 ± 0.014	0.003 ± 0.018	−0.001 ± 0.015	0.781	0.789	0.767	0.758	0.788	0.790
starQSM	0.004 ± 0.027	0.002 ± 0.027	0.002 ± 0.025	0.003 ± 0.022	0.004 ± 0.028	0.003 ± 0.024	0.756	0.778	0.738	0.786	0.787	0.780
NDI	0.002 ± 0.021	0.001 ± 0.022	0.001 ± 0.020	0.001 ± 0.018	0.003 ± 0.021	0.001 ± 0.021	0.786	0.784	0.763	0.793	0.794	0.812
ISDU-QSMNet-USW	**0.002 ± 0.018**	0.001 ± 0.019	**-0.001 ± 0.016**	-0.002 ± 0.015	**0.002 ± 0.019**	-0.002 ± 0.016	0.844	**0.839**	**0.825**	0.820	**0.854**	0.836
ROI: RIGHT GRAY MATTER												
COSMOS	−0.001 ± 0.022	−0.002 ± 0.024	−0.003 ± 0.019	0.000 ± 0.022	−0.001 ± 0.025	−0.003 ± 0.019	1.000	1.000	1.000	1.000	1.000	1.000
SpiNet	0.001 ± 0.019	−0.001 ± 0.019	−0.001 ± 0.016	0.000 ± 0.018	0.000 ± 0.019	0.000 ± 0.016	0.837	0.806	0.820	0.833	0.834	**0.838**
LPCNN	−0.001 ± 0.019	−0.002 ± 0.019	−0.003 ± 0.016	−0.002 ± 0.018	−0.003 ± 0.020	−0.001 ± 0.016	0.811	0.778	0.803	0.806	0.802	0.808
QSMNet	0.001 ± 0.017	0.000 ± 0.017	0.000 ± 0.015	0.000 ± 0.016	0.001 ± 0.017	−0.002 ± 0.015	0.786	0.771	0.772	0.780	0.784	0.787
DeepQSM	−0.001 ± 0.016	−0.001 ± 0.017	−0.002 ± 0.015	−0.001 ± 0.016	−0.001 ± 0.018	−0.003 ± 0.014	0.774	0.755	0.771	0.777	0.773	0.783
starQSM	0.002 ± 0.028	0.000 ± 0.028	0.000 ± 0.024	0.003 ± 0.025	0.001 ± 0.029	0.001 ± 0.024	0.760	0.757	0.718	0.797	0.767	0.773
NDI	0.001 ± 0.021	−0.001 ± 0.023	−0.001 ± 0.020	0.001 ± 0.020	0.000 ± 0.022	−0.001 ± 0.021	0.779	0.782	0.749	0.801	0.771	0.802
ISDU-QSMNet-USW	**-0.001 ± 0.019**	−0.003 ± 0.019	**-0.003 ± 0.016**	−0.002 ± 0.018	−0.003 ± 0.019	**-0.003 ± 0.016**	**0.845**	**0.814**	**0.823**	**0.838**	**0.837**	0.827

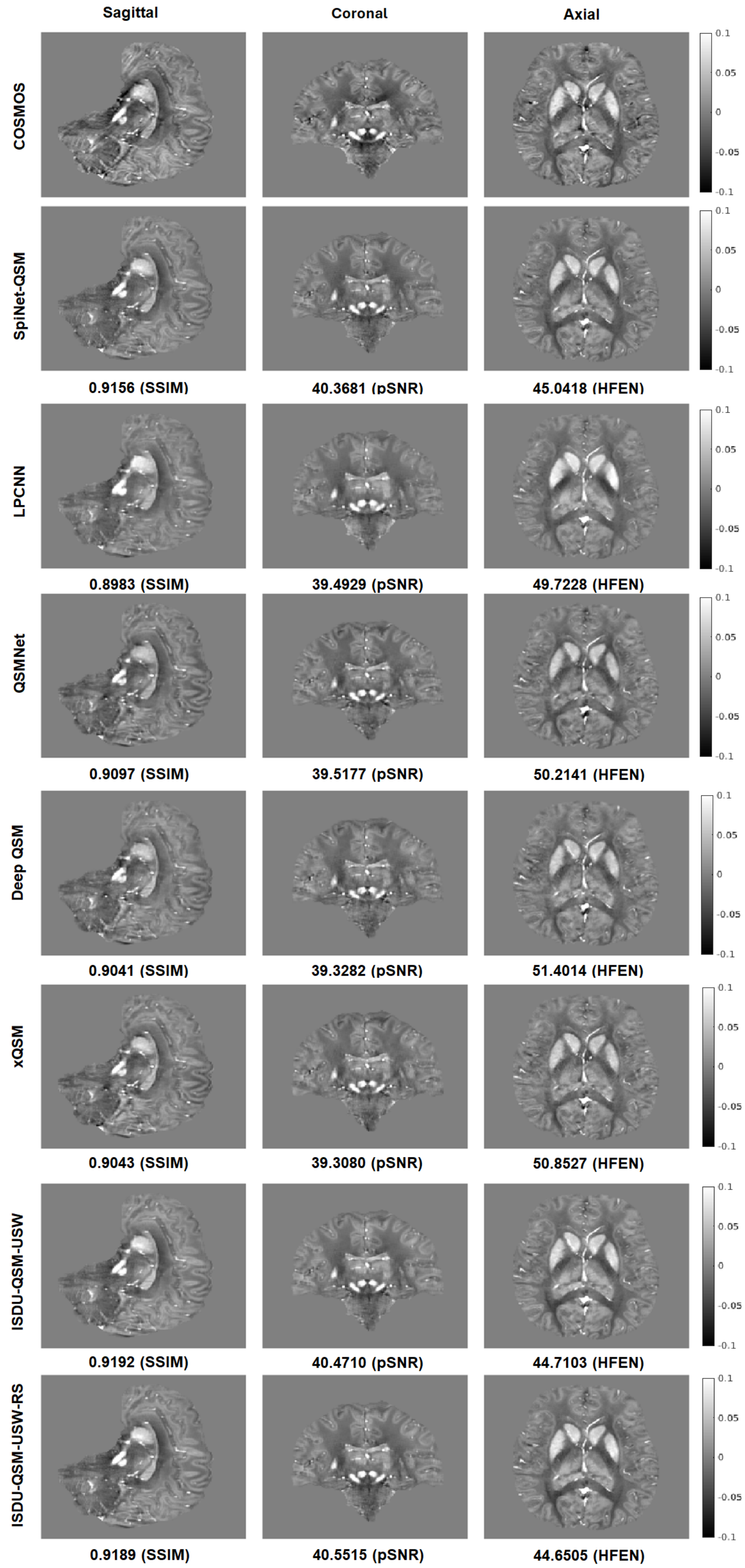

Figure 1: An example susceptibility image reconstructed from RC-1 data using models trained on the full dataset using SNU dataset. The first row shows the reference COSMOS maps in three orthogonal views: sagittal, coronal, and axial. Each subsequent row shows reconstructions from a different method: SpiNet-QSM, LPCNN, QSMnet, DeepQSM, xQSM, ISDU-QSMNet-USW, and ISDU-QSMNet-USW-RS. Each model row displays the same three views and includes quantitative evaluation metrics as x-axis labels—Structural Similarity Index Measure (SSIM), Peak Signal-to-Noise Ratio (PSNR), and High-Frequency Error Norm (HFEN)—computed with respect to the COSMOS reference.

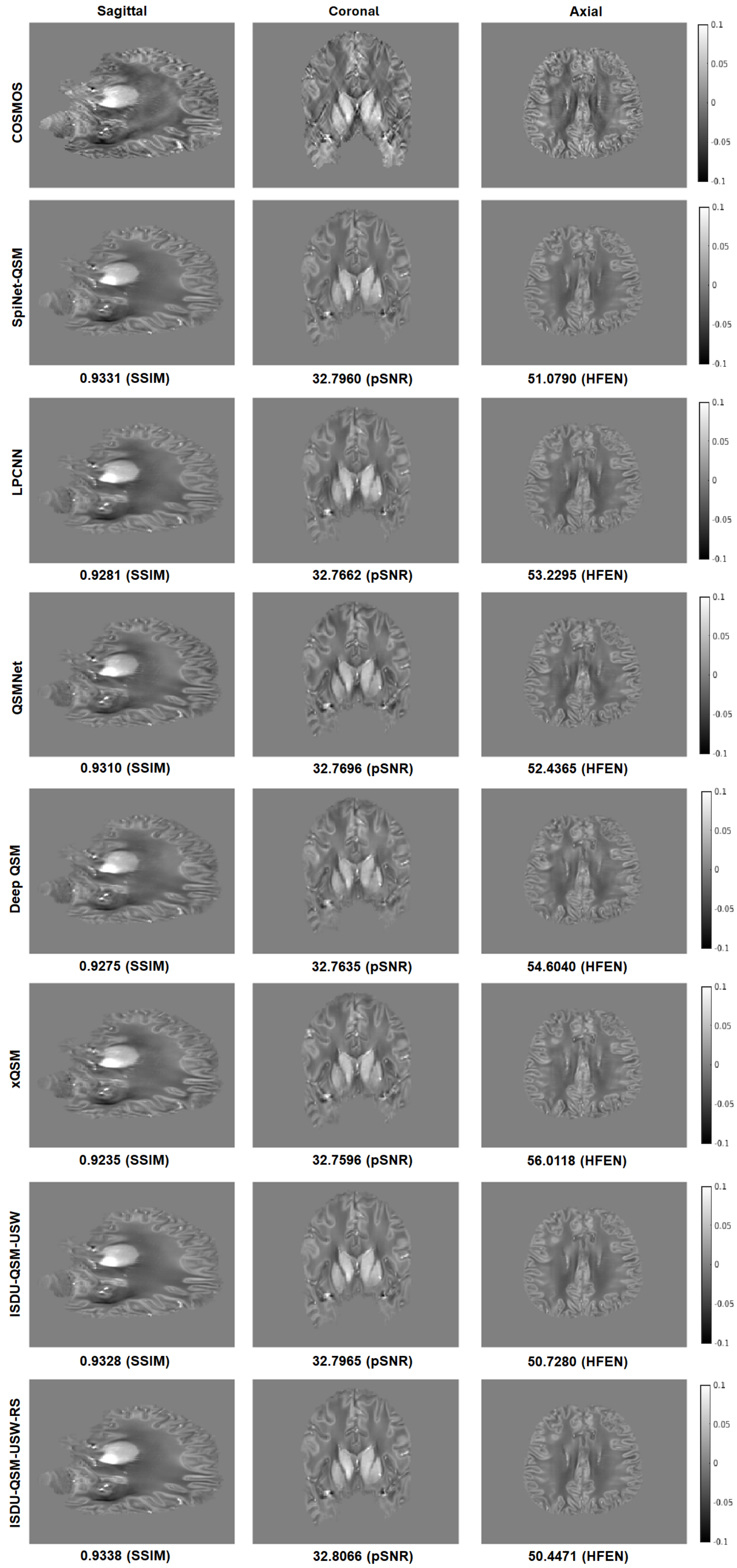

Figure 2: An example susceptibility image reconstructed from LPCNN data using models trained on the full dataset using SNU dataset. The first row shows the reference COSMOS maps in three orthogonal views: sagittal, coronal, and axial. Each subsequent row shows reconstructions from a different method: SpiNet-QSM, LPCNN, QSMnet, DeepQSM, xQSM, ISDU-QSMNet-USW, and ISDU-QSMNet-USW-RS. Each model row displays the same three views and includes quantitative evaluation metrics as x-axis labels—Structural Similarity Index Measure (SSIM), Peak Signal-to-Noise Ratio (PSNR), and High-Frequency Error Norm (HFEN)—computed with respect to the COSMOS reference.

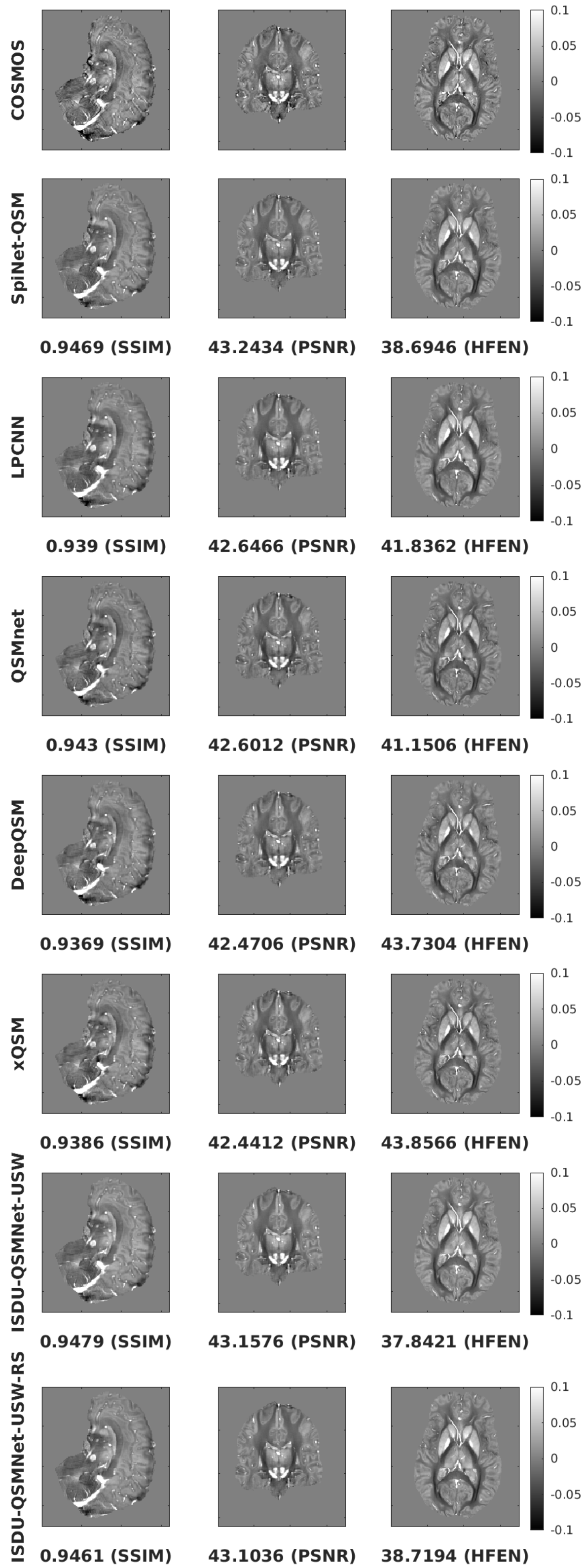

Figure 3: Comparison of Quantitative Susceptibility Mapping (QSM) reconstructions for subject-7 from the SNU dataset, across multiple models trained with the SNU dataset with full training data settings. The first row shows the reference COSMOS maps in three orthogonal views: sagittal, coronal, and axial. Each subsequent row shows reconstructions from a different method: SpiNet-QSM, LPCNN, QSMnet, DeepQSM, xQSM, ISDU-QSMNet-USW, and ISDU-QSMNet-USW-RS. Each model row displays the same three views and includes quantitative evaluation metrics as x-axis labels—Structural Similarity Index Measure (SSIM), Peak Signal-to-Noise Ratio (PSNR), and High-Frequency Error Norm (HFEN)—computed with respect to the COSMOS reference.

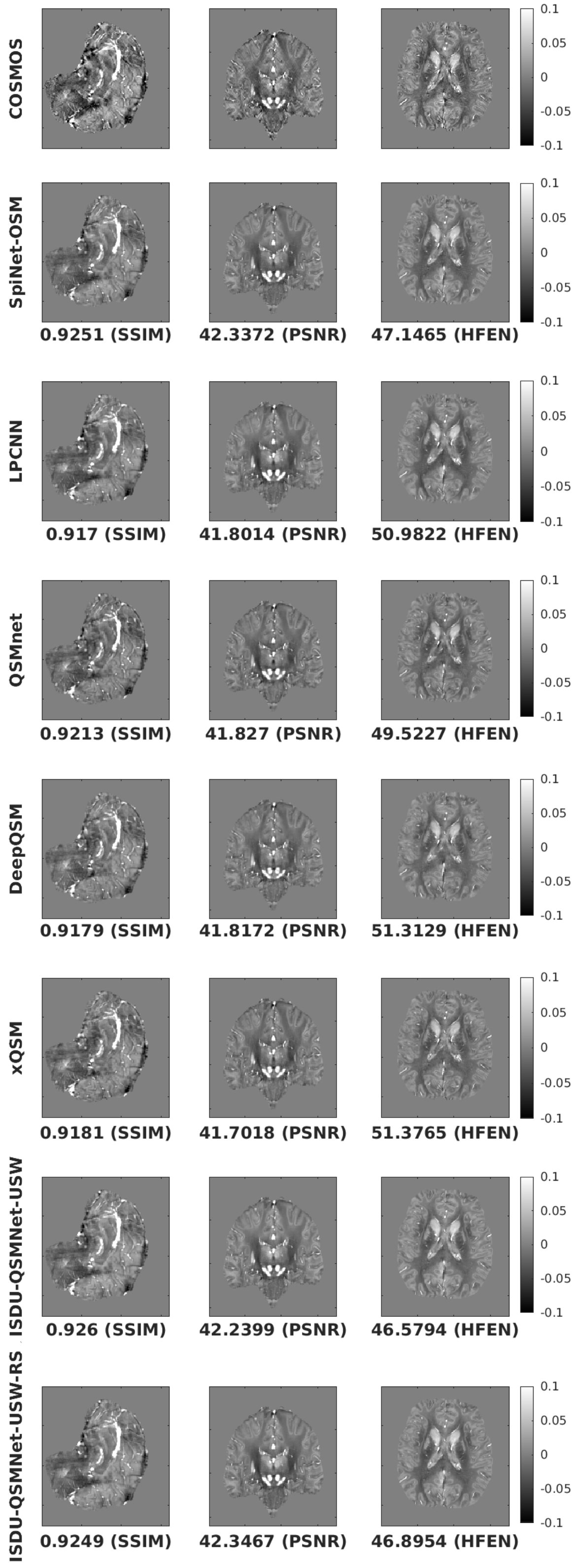

Figure 4: Comparison of Quantitative Susceptibility Mapping (QSM) reconstructions for subject-8 from the SNU dataset, across multiple models trained with the SNU dataset with full training data settings. The first row shows the reference COSMOS maps in three orthogonal views: sagittal, coronal, and axial. Each subsequent row shows reconstructions from a different method: SpiNet-QSM, LPCNN, QSMnet, DeepQSM, xQSM, ISDU-QSMNet-USW, and ISDU-QSMNet-USW-RS. Each model row displays the same three views and includes quantitative evaluation metrics as x-axis labels—Structural Similarity Index Measure (SSIM), Peak Signal-to-Noise Ratio (PSNR), and High-Frequency Error Norm (HFEN)—computed with respect to the COSMOS reference.

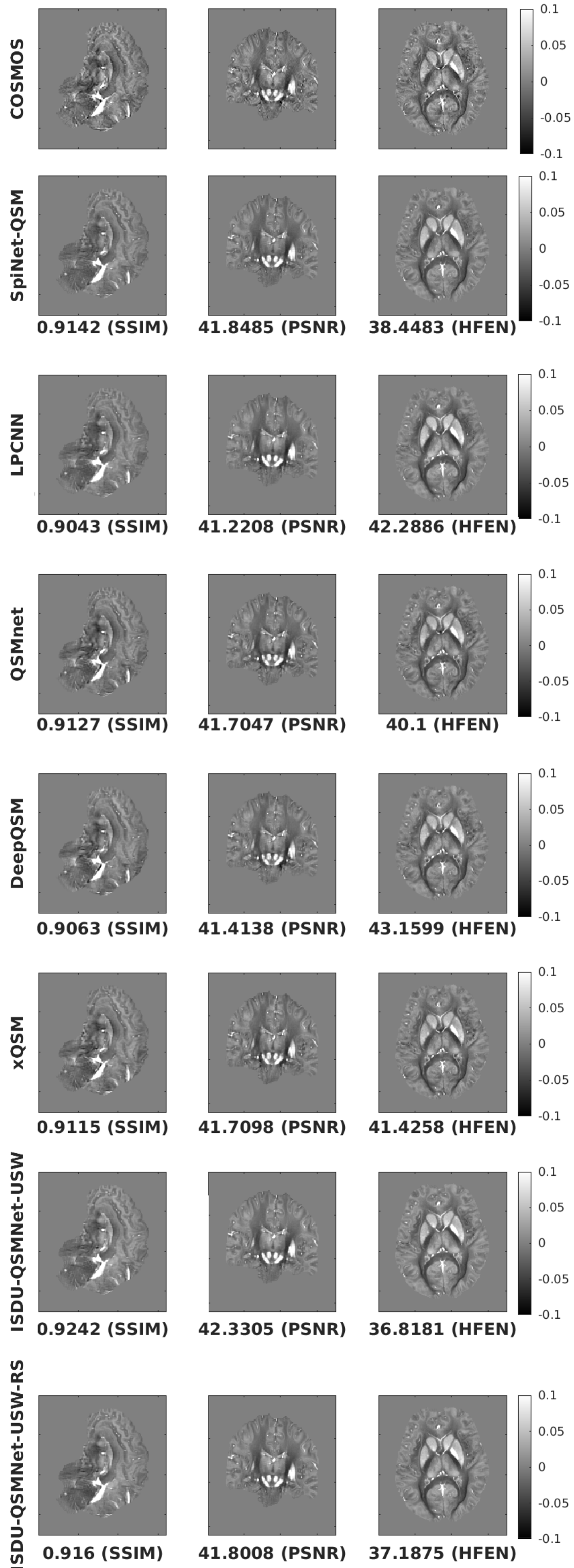

Figure 5: Comparison of Quantitative Susceptibility Mapping (QSM) reconstructions for subject-9 from the SNU dataset, across multiple models trained with the SNU dataset with full training data settings. The first row shows the reference COSMOS maps in three orthogonal views: sagittal, coronal, and axial. Each subsequent row shows reconstructions from a different method: SpiNet-QSM, LPCNN, QSMnet, DeepQSM, xQSM, ISDU-QSMNet-USW, and ISDU-QSMNet-USW-RS. Each model row displays the same three views and includes quantitative evaluation metrics as x-axis labels—Structural Similarity Index Measure (SSIM), Peak Signal-to-Noise Ratio (PSNR), and High-Frequency Error Norm (HFEN)—computed with respect to the COSMOS reference.

6 Effect of Denoiser Architecture in ISDU-QSMNet

To investigate the impact of denoising network architecture on QSM reconstruction quality, we evaluated the performance of the proposed ISDU-QSMNet using four different denoiser backbones: a simple Wide ResNet CNN, UNet-mini, UNet-heavy, and WideResNet-18. Figure 6 shows representative QSM reconstructions for Subject 8 from the SNU dataset, highlighting the visual differences across these architectures. Among the tested configurations, the WideResNet-18 denoiser produced the most accurate and structurally consistent reconstructions, effectively preserving fine anatomical details while suppressing noise and artifacts. This superior performance led to the selection of WideResNet-18 as the denoising architecture for ISDU-QSMNet.

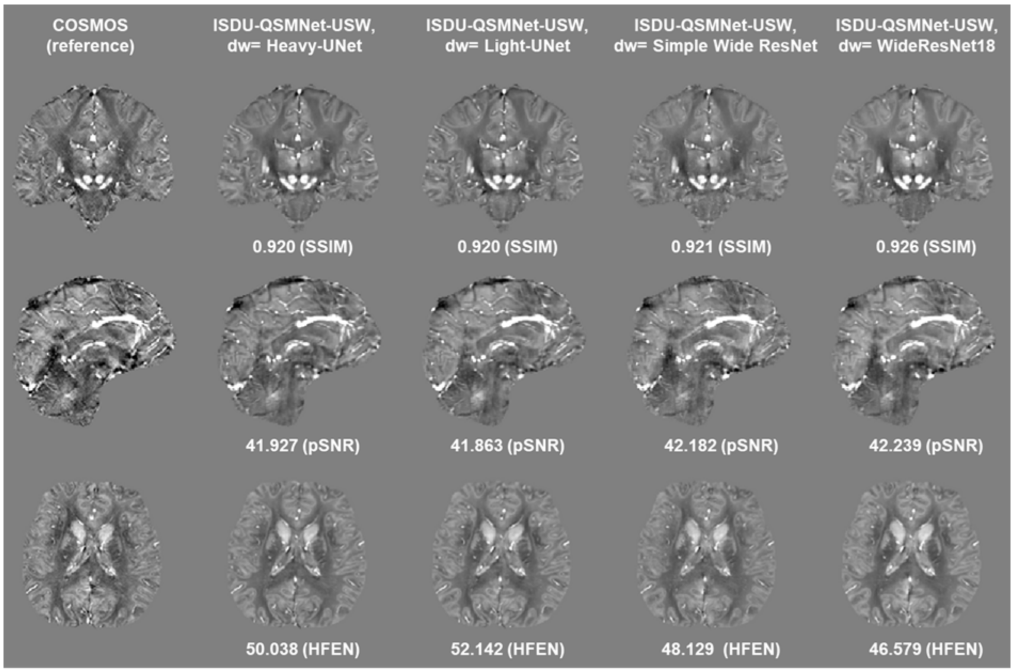

Figure 6: Sample QSM reconstructions for Subject 8 from the SNU dataset, obtained using the proposed ISDU-QSMNet with different denoising networks: Simple Wide ResNet CNN, UNet-mini, UNet-heavy, and WideResNet-18. WideResNet-18 demonstrates the best reconstruction quality, leading to its selection as the denoising network for ISDU-QSMNet.

References

[1] Jaeyeon Yoon, Enhao Gong, Itthi Chatnuntawech, Berkin Bilgic, Jingu Lee, Woojin Jung, Jingyu Ko, Hosan Jung, Kawin Setsompop, Greg Zaharchuk, et al. Quantitative susceptibility mapping using deep neural network: Qsmnet. *Neuroimage*, 179:199–206, 2018.

[2] Kuo-Wei Lai, Manisha Aggarwal, Peter van Zijl, Xu Li, and Jeremias Sulam. Learned proximal networks for quantitative susceptibility mapping. In *Medical Image Computing and Computer Assisted Intervention–MICCAI 2020: 23rd International Conference, Lima, Peru, October 4–8, 2020, Proceedings, Part II 23*, pages 125–135. Springer, 2020.

[3] Stephen M Smith. Fast robust automated brain extraction. *Human brain mapping*, 17(3):143–155, 2002.

[4] Wei Li, Bing Wu, and Chunlei Liu. Quantitative susceptibility mapping of human brain reflects spatial variation in tissue composition. *Neuroimage*, 55(4):1645–1656, 2011.

[5] Bing Wu, Wei Li, Arnaud Guidon, and Chunlei Liu. Whole brain susceptibility mapping using compressed sensing. *Magnetic resonance in medicine*, 67(1):137–147, 2012.

[6] Pinar Senay Özbay, Andreas Deistung, Xiang Feng, Daniel Nanz, Jürgen Rainer Reichenbach, and Ferdinand Schweser. A comprehensive numerical analysis of background phase correction with v-sharp. *NMR in Biomedicine*, 30(4):e3550, 2017.

[7] Mark Jenkinson, Peter Bannister, Michael Brady, and Stephen Smith. Improved optimization for the robust and accurate linear registration and motion correction of brain images. *Neuroimage*, 17(2):825–841, 2002.

[8] Mark Jenkinson and Stephen Smith. A global optimisation method for robust affine registration of brain images. *Medical image analysis*, 5(2):143–156, 2001.

[9] Tian Liu, Pascal Spincemaille, Ludovic De Rochefort, Bryan Kressler, and Yi Wang. Calculation of susceptibility through multiple orientation sampling (cosmos): a method for conditioning the inverse problem from measured magnetic field map to susceptibility source image in mri. *Magnetic Resonance in Medicine: An Official Journal of the International Society for Magnetic Resonance in Medicine*, 61(1):196–204, 2009.